Supporting Information

CO_2 Hydrogenation to Methanol Catalyzed by Mn-SNS Complex: Role of *fac/mer* Isomerism on Catalytic Reactivities

Sai V. C. Vummaleti,[1,2,§] Huiwen Tan,[1,§] Jingyi Liu,[1] and Xinglong Zhang[1,*]

[1] Dr. S. V. C. Vummaleti, H. Tan, J. Liu, Prof. Dr. X. Zhang
Department of Chemistry
The Chinese University of Hong Kong
Shatin, New Territories, Hong Kong, China
E-mail: xinglong.zhang@cuhk.edu.hk

[2] Dr. S. V. C. Vummaleti
Institute of High Performance and Computing (IHPC)
Agency for Science, Technology and Research (A*STAR)
1 Fusionopolis Way, #16-16 Connexis, Singapore 138632, Republic of Singapore

§ These authors contributed equally.

Content

Section S1. Thermodynamic stability of Mn-*fac* and Mn-*mer* isomers

Mn-*fac*	Mn-*mer*
ΔΔG = 0.0 (0.0) kcal/mol	ΔΔG = 2.2 (1.4) kcal/mol
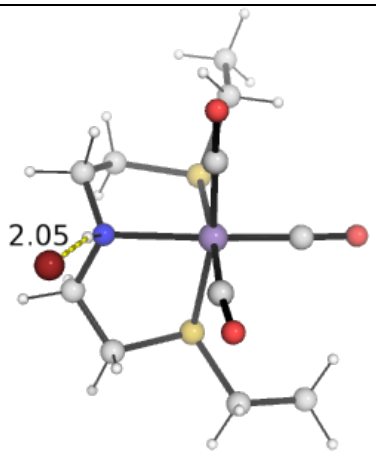	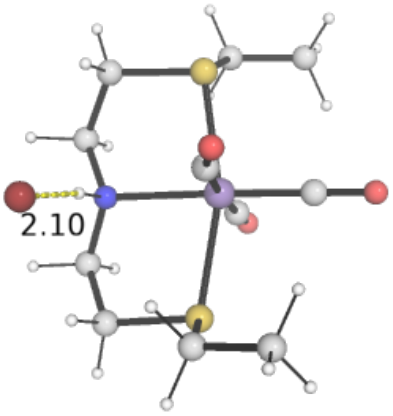

Figure S1. DFT optimized geometries of precatalyst **Mn-*fac*** and its less stable isomer, **Mn-*mer***. Key bond distance is given in Å. Gibbs energies were computed at SMD(THF)-B3LYP-D3BJ/def2-QZVP//B3LYP-D3BJ/(def2-TZVPPD for Mn and Br^- + def2-SVP for all other atoms) level of theory. Corresponding free energies computed at the SMD(THF)-MN15/def2-QZVP//B3LYP-D3BJ/(def2-TZVPPD for Mn and Br^-, def2-SVP for all other atoms) level are given in parentheses.

Section S2. Hydrogenation of CO_2 to HCOOH mediated by 1-*mer*

We explored both ligand-assisted and ligand-participated mechanisms for CO_2 hydrogenation to HCOOH mediated by **1-*mer***, with a focus on the involvement of the N–H functionality of the SNS ligand. The computed Gibbs free energy profiles for the corresponding pathways are shown in Figures S2 and S3, respectively.

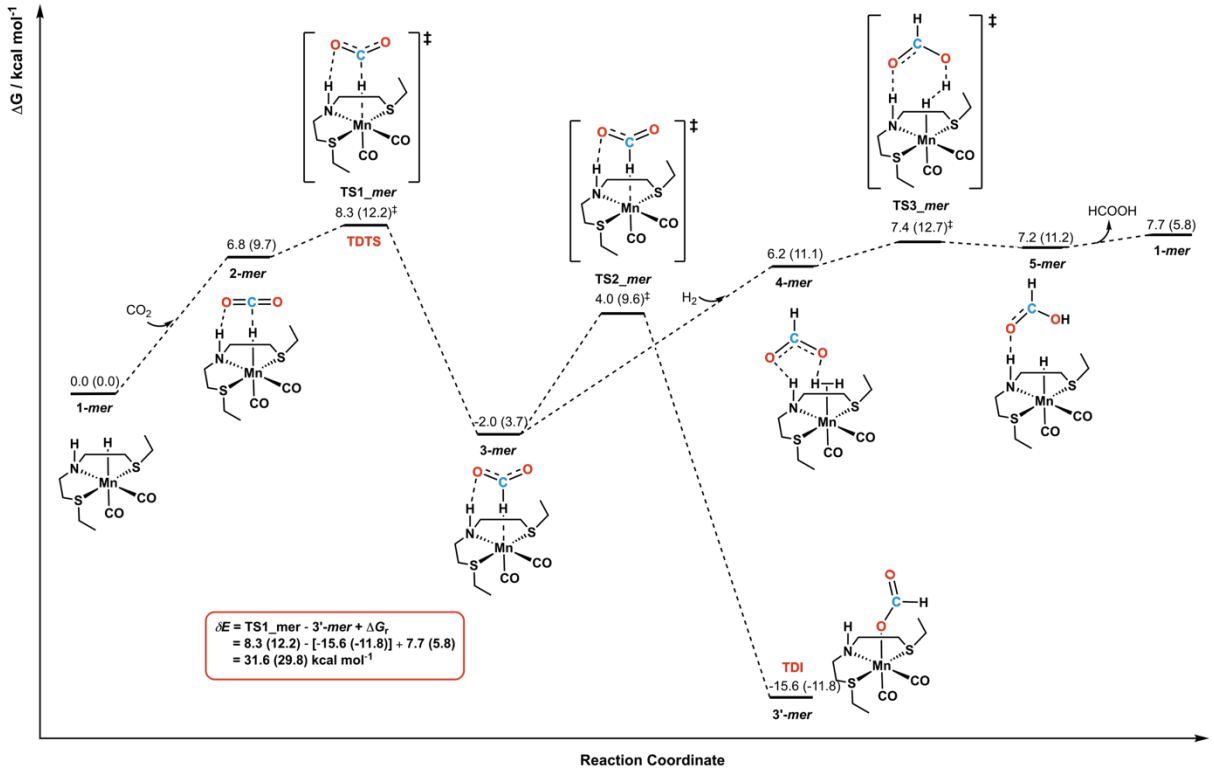

Figure S2. Gibbs free energy profile for CO_2 hydrogenation to HCOOH via ligand-assisted pathway mediated by **1-*mer***. The free energies were computed at SMD(THF)-B3LYP-D3BJ/def2-QZVP//B3LYP-D3BJ/(def2-TZVPPD for Mn + def2-SVP for all other atoms) level of theory. Corresponding free energies computed at the SMD(THF)-MN15/def2-QZVP//B3LYP-D3BJ/(def2-TZVPPD for Mn, def2-SVP for all other atoms) level are given in parentheses. All values are given in kcal/mol with respect to **1-*mer***, and all other substrates. TDI, turnover frequency-determining intermediate; TDTS, turnover frequency-determining transition state.

Ligand-assisted pathway. The mechanism for the ligand-assisted pathway begins with the coordination of CO_2 to complex **1-*mer***, forming intermediate **2-*mer***, where CO_2 is hydrogen-bonded to the H atom of the amine group in **1-*mer***, Figure S2. This step is endergonic, with **2-*mer*** lying 6.8 (9.7) kcal/mol above **1-*mer***. From **2-*mer***, the next step involves the hydride transfer from the Mn center to the carbon atom of CO_2, forming a stable intermediate **3-*mer***, which lies 8.8 (6.0) kcal/mol below **2-*mer***. This step proceeds through **TS1_*mer***, with an activation free energy barrier of 1.5 (2.5) kcal/mol from complex **2-*mer***. Intermediate **3-*mer*** can isomerize to a more stable intermediate **3′-*mer***, lying 13.6 (15.5) kcal/mol below **3-*mer*** and requires overcoming an activation barrier of 6.0 (5.9) kcal/mol via **TS2_*mer***, Figure S2. It

is worth noting that the highly stabilized intermediate **3′-*mer*** is the resting state of the catalytic cycle. Alternatively, intermediate **3-*mer*** may react directly with H_2 in an endergonic fashion, forming intermediate **4-*mer***, which lies 8.2 (7.4) kcal/mol above **3-*mer***. From **4-*mer***, heterolytic cleavage of H_2 and the concerted transfer of a proton to the formate moiety yields intermediate **5-*mer***, in which the product HCOOH is hydrogen-bonded to the metal complex via the H atom of the amine group, Figure S2. This step is kinetically facile and proceeds through **TS3_*mer***, with a low activation free energy barrier of 1.2 (1.6) kcal/mol from complex **4-*mer***, Figure S2. Finally, the release of product HCOOH regenerates the starting species **1-*mer***, thus closing the catalytic cycle.

Having established the catalytic cycle, we evaluate the energetic span (δE) by identifying the turnover frequency (TOF) determining intermediate, TDI, and the TOF-determining transition state, TDTS. From Figure S2, it is evident that **3′-*mer*** serves as the TDI, being the most stable intermediate in the cycle, while among the transition states, **TS1_*mer*** is identified as the TDTS as it maximizes δE due to its position prior to the TDI, thereby incorporating the reaction free energy, ΔG_r. The catalytic cycle shows an overall δE of 31.6 (29.8) kcal/mol, which is higher by 3.3 (1.8) kcal/mol than the corresponding **1-*fac*** pathway (δE = 28.3 (28.0) kcal/mol; Figure 3 in the main text), indicating that the **1-*mer*** pathway is kinetically less favorable under the experimental reaction conditions (120 °C and 10 atm H_2).

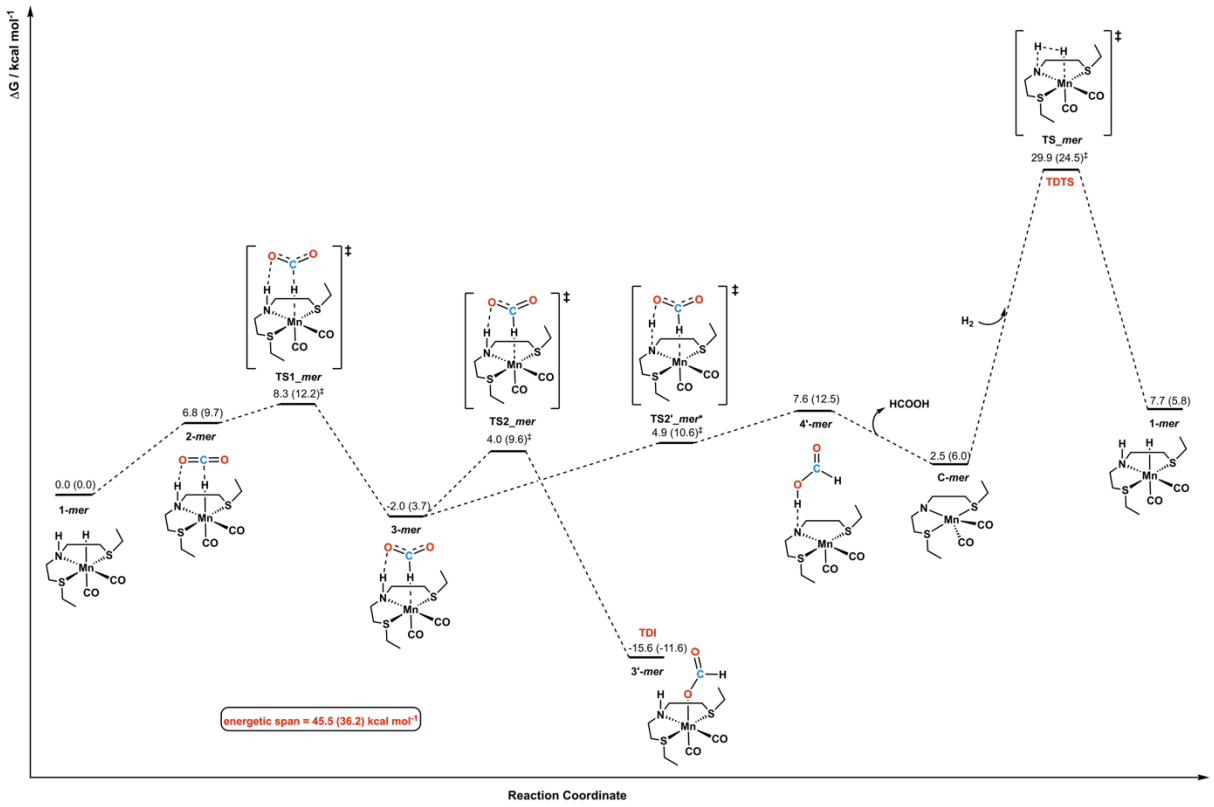

Figure S3. Gibbs free energy profile for CO_2 hydrogenation to HCOOH via ligand-participated pathway mediated

by **1-*mer***. The free energies were computed at SMD(THF)-B3LYP-D3BJ/def2-QZVP//B3LYP-D3BJ/(def2-TZVPPD for Mn + def2-SVP for all other atoms) level of theory. Corresponding free energies computed at the SMD(THF)-MN15/def2-QZVP//B3LYP-D3BJ/(def2-TZVPPD for Mn, def2-SVP for all other atoms) level are given in parentheses. All values are given in kcal/mol with respect to **1-*mer***, and all other substrates. TDI, turnover frequency-determining intermediate; TDTS, turnover frequency-determining transition state. **TS2′_*mer**** was obtained from a constrained ModRedundant optimization of the O-H and N-H distances and is used as an approximate transition-state structure.

Ligand-participated pathway. Alternatively, from **3-*mer***, proton transfer to the formate group mediated by the N–H functionality yields intermediate **4′-*mer***, in which the product HCOOH is hydrogen-bonded to the metal complex via the H atom of the amine group, Figure S3. This step is endergonic, with **4′-*mer*** lying 9.6 (8.8) kcal/mol above **3-*mer*** and proceeds via **TS2′_*mer**** with an activation free energy barrier of 6.9 (6.9) kcal/mol, Figure S3. Next, the release of product HCOOH generates **C-*mer***, which lies 5.1 (6.5) kcal/mol below **4′-*mer*.** Subsequent heterolytic cleavage of H_2 at the vacant site of **C-*mer*** via **TS_*mer***, with an activation barrier of 27.4 (18.5) kcal/mol, regenerates the active species **1-*mer***, thereby closing the catalytic cycle, Figure S3. This pathway exhibits an overall δE of 45.5 (36.2) kcal/mol, which is ~14.0 (6.4) kcal/mol higher in energy than the ligand-assisted pathway, indicating that this pathway is not operative.

Section S3. Hydrogenation of *N*-formylmorpholine to methanol mediated by 1-*fac*

In this section, we discuss in detail the hydrogenation of *N*-formylmorpholine (**14**) to methanol catalyzed by complex **1-*fac***, exploring two alternative pathways: Pathway A (C=O bond hydrogenation followed by C–N bond hydrogenation; Figure S4) and Pathway B (C–N bond hydrogenation followed by C=O bond hydrogenation; Figure S5).

C=O hydrogenation followed by C–N hydrogenation. The interaction between complex **1-*fac*** and **14** forms intermediate **15-*fac***, where the carbonyl group of the amide is hydrogen-bonded to **1-*fac***, Figure S4. This step is endergonic, with **15-*fac*** lying 9.2 (10.9) kcal/mol above **1-*fac***. Next, the concerted transfer of hydridic and protonic hydrogen atoms to the carbon and oxygen atoms of **14**, respectively, occurs via **TS4_*fac***, with an activation free energy barrier of 21.4 (22.1) kcal/mol from complex **15-*fac***, leading to the formation of intermediate **16-*fac***, Figure S4. The slightly exergonic release of hydrogenated *N*-formylmorpholine from **16-*fac*** yields the penta-coordinated intermediate **C-*fac***, which lies 3.1 (3.7) kcal/mol below **16-*fac***. From **C-*fac***, coordination of a H_2 molecule at the vacant metal site and its subsequent heterolytic cleavage regenerates the active species **1-*fac***. This highly exergonic step, with **1-*fac*** lying 15.7 (20.4) kcal/mol below **C-*fac***, proceeds via **TS_*fac***, which requires an activation free energy barrier of 13.9 (4.7) kcal/mol from **C-*fac***, Figure S4.

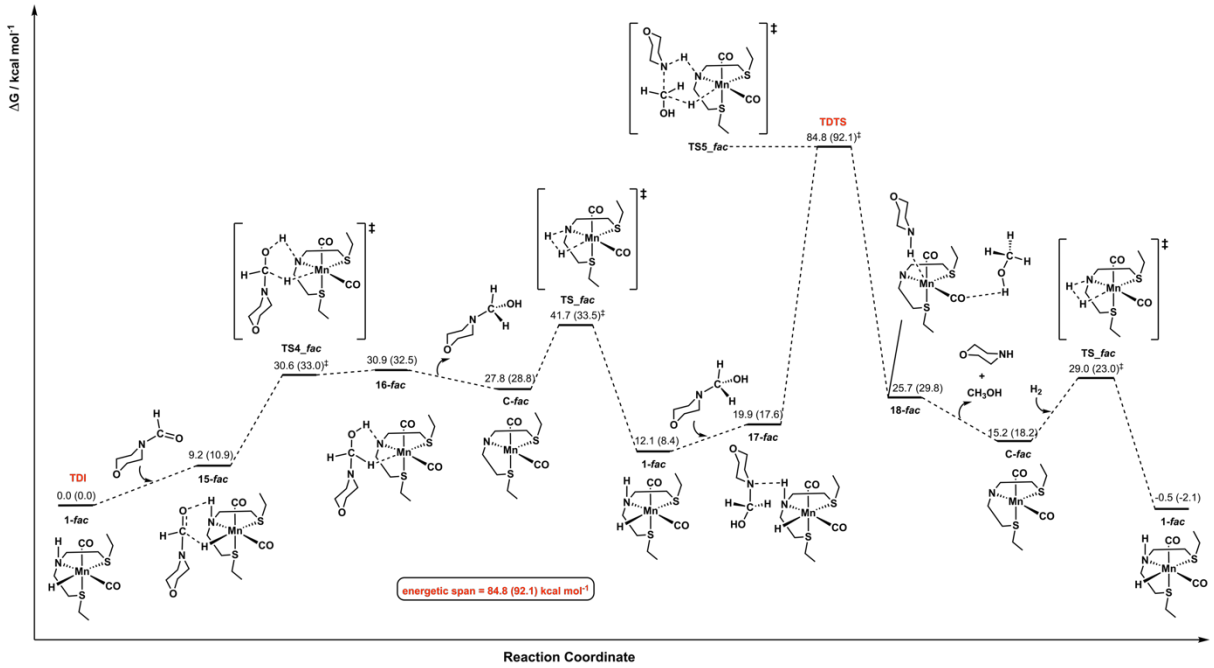

Figure S4. Gibbs free energy profile for *N*-formylmorpholine hydrogenation to methanol via Pathway A (C=O bond hydrogenation followed by C–N bond hydrogenation) mediated by **1-*fac***. The free energies were computed at SMD(THF)-B3LYP-D3BJ/def2-QZVP//B3LYP-D3BJ/(def2-TZVPPD for Mn + def2-SVP for all other atoms) level of theory. Corresponding free energies computed at the SMD(THF)-MN15/def2-QZVP//B3LYP-D3BJ/(def2-TZVPPD for Mn, def2-SVP for all other atoms) level are given in parentheses. All values are given

in kcal/mol with respect to **1-*fac***, and all other substrates.

The hydrogenated *N*-formylmorpholine then re-enters the pathway by interacting with **1-*fac*** to form complex **17-*fac***, which lies 7.8 (9.2) kcal/mol above **1-*fac***, Figure S4. Finally, the dissociation of the C–N bond in **17-*fac*** occurs through a concerted mechanism involving the simultaneous transfer of hydridic and protonic hydrogen atoms to the carbon and nitrogen atoms, respectively, yielding complex **18-*fac***, where the product methanol and regenerated morpholine are weakly coordinated to the metal complex via hydrogen bonds. This step proceeds via **TS5_*fac*** with a notably high activation free energy barrier of 64.9 (74.5) kcal/mol, indicating that it is the rate-determining step for the hydrogenation of *N*-formylmorpholine to methanol, Figure S4. Interestingly, the DFT study by Mandal *et al.* did not report this specific step but identified the heterolytic cleavage of H_2 as the rate-determining step for this proposed pathway. Next, the release of methanol and morpholine from **18-*fac*** into the gas phase, in a slightly exergonic step, returns the system to **C-*fac***, which is 10.5 (11.6) kcal/mol lower than **18-*fac***. Subsequent coordination and cleavage of H_2 regenerate the active species **1-*fac***, completing the catalytic cycle.

Figure S4 shows that **TS5_*fac*** is identified as the TDTS, while **1-*fac*** serves as the TDI, giving a significantly high δE of 84.8 (92.1) kcal/mol, indicating that this pathway is unlikely to operate under the experimental conditions (120 °C and 10 atm H_2).

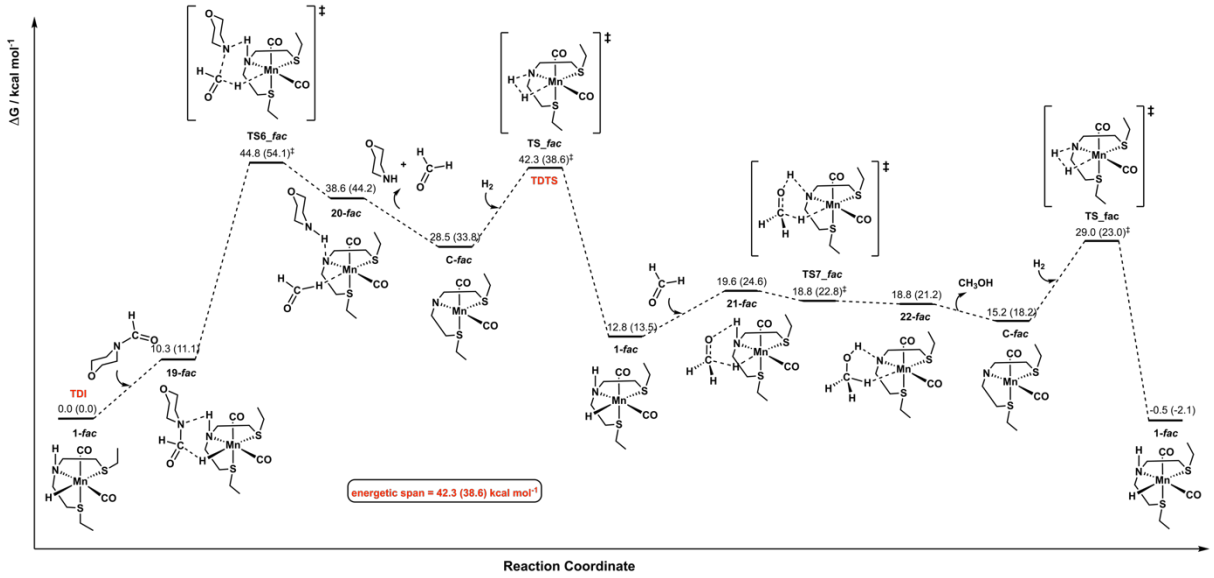

Figure S5. Gibbs free energy profile for *N*-formylmorpholine hydrogenation to methanol via Pathway B (C–N bond hydrogenation followed by C=O bond hydrogenation) mediated by **1-*fac***. The free energies were computed at SMD(THF)-B3LYP-D3BJ/def2-QZVP//B3LYP-D3BJ/(def2-TZVPPD for Mn + def2-SVP for all other atoms) level of theory. Corresponding free energies computed at the SMD(THF)-MN15/def2-QZVP//B3LYP-D3BJ/(def2-TZVPPD for Mn, def2-SVP for all other atoms) level are given in parentheses. All values are given

in kcal/mol with respect to **1-*fac***, and all other substrates.

C–N hydrogenation followed by C=O hydrogenation. In an alternative route, **1-*fac*** coordinates *N*-formylmorpholine to form complex **19-*fac***, where the C–N group of the amide moiety is hydrogen-bonded to **1-*fac***, which lies 10.3 (11.1) kcal/mol above **1-*fac***, Figure S5. Next, a concerted dissociation of the C–N bond, accompanied by simultaneous transfer of hydridic and protonic hydrogen atoms to the carbon and nitrogen atoms, respectively, leads to complex **20-*fac***, where the morpholine and formaldehyde are hydrogen-bonded to the metal complex, Figure S5. This step proceeds via **TS6_*fac***, with an activation free energy barrier of 34.5 (43.0) kcal/mol from complex **19-*fac***. The subsequent release of these products leads to **C-*fac***, which lies 10.1 (10.4) kcal/mol below **20-*fac***. Coordination of H_2 to **C-*fac***, followed by its heterolytic cleavage, regenerates the active species **1-*fac***, Figure S5. Subsequently, formaldehyde re-enters the catalytic cycle and forms complex **21-*fac*** upon its interaction with **1-*fac***. This step is endergonic, with **21-*fac*** lying 6.8 (11.1) kcal/mol above **1-*fac***. In the final step, a concerted transfer of hydridic and protonic hydrogen atoms to the carbon and oxygen atoms of formaldehyde produces complex **22-*fac***, where the desired product methanol is hydrogen-bonded to the metal complex, Figure S5. The release of methanol into the gas phase in a slightly exergonic step returns the system to **C-*fac***, which lies 3.6 (3.0) kcal/mol below **22-*fac***. Subsequent coordination of H_2 and its heterolytic cleavage at the Mn center in **C-*fac*** regenerates **1-*fac***, completing the catalytic cycle.

For the studied catalytic cycle, **TS_*fac*** serves as the TDTS, with **1-*fac*** as the TDI. The δE is calculated to be 42.3 (38.6) kcal/mol, which is significantly lower by 42.5 (53.5) kcal/mol than for the competing pathway via C=O bond hydrogenation followed by C–N bond (δE = 84.8 (92.1) kcal/mol). This energetic span is, however, higher by 7.3 (6.3) kcal/mol than that of the corresponding **1-*mer*** pathway (δE = 35.0 (32.3) kcal/mol), indicating that **1-*mer*** serves as the active hydride species for the hydrogenation of *N*-formylmorpholine to methanol, see Figure 7 in the main text.

Section S4. Distortion-interaction analysis for H_2-coordinated intermediates

Distortion-interaction analysis is applied to H_2-coordinated intermediates (**C-*fac*-H₂** and **C-*mer*-H₂**) to discern the factors affecting stability.

The H_2-coordinated intermediate structures are decomposed by dividing the Mn(0) complex (**C-*fac*** and **C-*mer***), and H_2 as components. Single point calculations with SMD(THF) solvent correction were performed at B3LYP-D3BJ/def2-QZVP level of theory to obtain distortion and interaction energies.

The distortion energy is given by:

$$E_{dist} = E_{INT,frag1} + E_{INT,frag2} - (E_{eq,frag1} + E_{eq,frag2})$$

where *INT,frag1,2* represent individual fragments in their distorted intermediate geometries; and *eq,frag1,2* represent individual fragments in their optimized, equilibrium ground-state geometries; the interaction energy is given by:

$$E_{int} = E_{INT} - (E_{INT,frag1} + E_{INT,frag2})$$

which accounts for the stabilizing interactions (e.g., electrostatic, orbital, dispersion) between the distorted fragments in the intermediate.

Thus, the total stabilization energy is given by:

$$\Delta E = E_{dist} + E_{int.}$$

Note that this single point activation energy and the activation energy differences $\Delta\Delta E^{\ddagger}$ between the intermediates (**C-*fac*-H₂** vs. **C-*mer*-H₂**) may be different from the Gibbs energy differences $\Delta\Delta G^{\ddagger}$ that is computed fully (including vibrational frequencies analysis) at SMD(THF)-B3LYP-D3BJ/def2-QZVP//B3LYP-D3BJ/(def2-TZVPPD for Mn + def2-SVP for all other atoms) and SMD(THF)-MN15/def2-QZVP//B3LYP-D3BJ/(def2-TZVPPD for Mn + def2-SVP for all other atoms) levels, respectively. The MN15 values are given in parentheses.

Distortion–interaction analysis highlights a clear difference in the stabilization of the H_2-coordinated intermediates. The analysis shows that **C-*fac*-H₂** exhibits a lower distortion energy (4.7 (5.3) kcal/mol) than **C-*mer*-H₂** (9.4 (10.3) kcal/mol), along with a more stabilizing interaction energy (–9.8 (–19.7) vs –0.2 (–9.1) kcal/mol). As a result, **C-*fac*-H₂** presents a lower overall $\Delta E^{\ddagger}$ relative to **C-*mer*-H₂** (–5.1 (–14.4) kcal/mol vs. 9.2 (1.2) kcal/mol), Table S1.

Table S1. Distortion-interaction analysis.

Intermediate	ΔE	E_{dist}	E_{int}
C-*fac*-H₂	–5.1 (–14.4)	4.7 (5.3)	–9.8 (–19.7)

C-*mer*-H_2	9.2 (1.2)	9.4 (10.3)	–0.2 (–9.1)

Section S5. Ligand environment effects on heterolytic H_2 activation in the model systems

To probe the influence of the ligand *trans* to H_2 molecule, we examined model systems in which the CO ligand *trans* to H_2 in **C-*mer*** was replaced with ligands of varying π-acceptor strengths (H_2O, PH_3, PF_3) and evaluated both the stability of the resulting H_2-coordinated intermediates and the corresponding heterolytic H_2 cleavage barriers. The stability of the H_2-coordinated intermediates follows the π-acceptor strength of the *trans* ligand: **C-*mer*-H_2_H_2O** (10.3 (2.1) kcal/mol) < **C-*mer*-H_2_PH_3** (17.5 (9.7) kcal/mol) < **C-*mer*-H_2** (20.1 (12.1) kcal/mol) < **C-*mer*-H_2_PF_3** (22.3 (15.8) kcal/mol), Figure S6, which directly correlates with the corresponding H_2 cleavage barriers: **TS_*mer*_H_2O** (18.4 (10.4) kcal/mol) < **TS_*mer*_PH_3** (23.7 (16.3) kcal/mol) < **TS_*mer*** (27.4 (18.5) kcal/mol) ≈ **TS_*mer*_PF_3** (26.9 (20.9) kcal/mol), Figure S7.

C-*mer*-H_2_H_2O	**C-*mer*-H_2_PH_3**
ΔG = 10.3 (2.1) kcal/mol	ΔG = 17.5 (9.7) kcal/mol
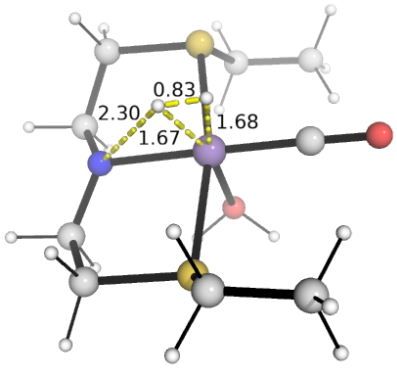	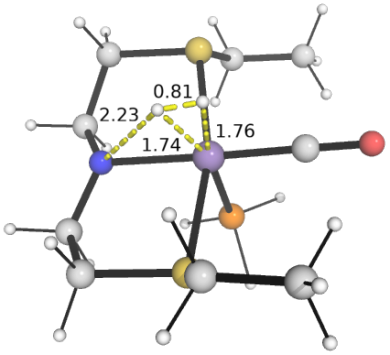
C-*mer*-H_2	**C-*mer*-H_2_PF_3**
ΔG = 20.1 (12.1) kcal/mol	ΔG = 22.3 (15.8) kcal/mol
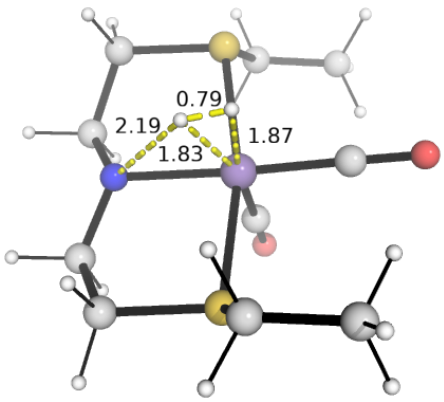	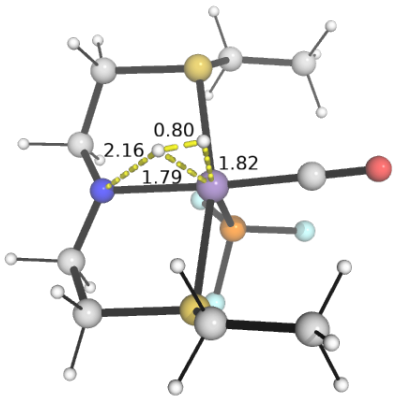
C-*mer*-H_2-PNP	

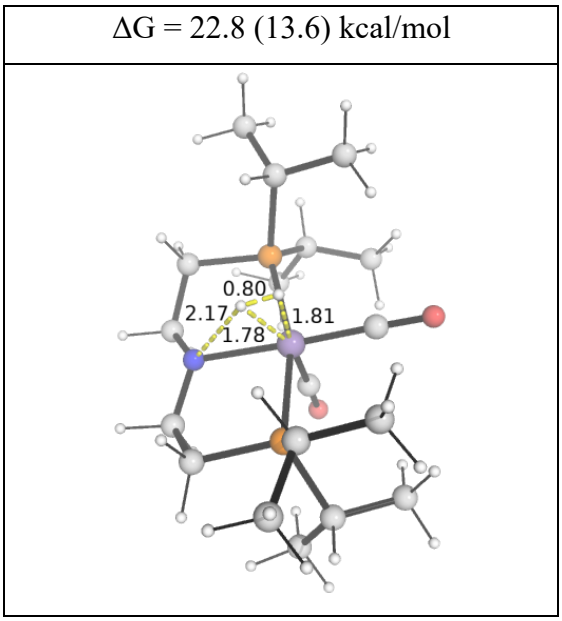

Figure S6. DFT optimized geometries of H_2-coordinated intermediates for the *mer*-Mn-SNS model systems, where the CO ligand *trans* to the H_2 coordination site is replaced by ligands of varying π-acceptor strength (H_2O, PH_3, PF_3), along with the literature-reported Mn-PNP system (**C-*mer*-H₂-PNP**). Gibbs energies are reported relative to the corresponding **C-*mer*** complexes. Selected bond distances are given in Å. Gibbs energies were computed at SMD(THF)-B3LYP-D3BJ/def2-QZVP//B3LYP-D3BJ/(def2-TZVPPD for Mn + def2-SVP for all other atoms) level of theory. Corresponding free energies computed at the SMD(THF)-MN15/def2-QZVP//B3LYP-D3BJ/(def2-TZVPPD for Mn, def2-SVP for all other atoms) level are given in parentheses.

These energetic trends are further supported by the structural parameters of the H_2-coordinated intermediates for the model systems. In **C-*mer*-H₂_H₂O**, corresponding to a σ-donor ligand, increased electron density at the Mn center (Δq(Mn) = –0.43) is associated with relatively short Mn–H distances (~1.68 Å) and a slightly elongated H–H′ bond (0.83 Å), Figure S6. In contrast, **C-*mer*-H₂_PH₃**, containing a weak π-acceptor ligand, the reduced electron density (Δq(Mn) = –0.37) results in longer Mn–H distances (1.74–1.76 Å) and a shorter H–H′ bond (0.81 Å). Consistent with this trend, in **C-*mer*-H₂**, containing the π-acceptor CO ligand, the electron density at Mn further decreases (Δq(Mn) = –0.32), accompanied by longer Mn–H distances (1.83–1.87 Å) and a shorter H–H′ bond (0.79 Å). Interestingly, in **C-*mer*-H₂_PF₃**, a strong π-acceptor ligand, the electron density at Mn (Δq(Mn) = –0.35) is intermediate, with corresponding Mn–H distances (1.79–1.82 Å) and a H–H′ bond length of 0.80 Å, Figure S6. In addition, the protonic hydrogen atom (H′) is positioned progressively closer to the amido nitrogen center, with N···H′ distances decreasing from 2.30 Å (H_2O) to 2.23 Å (PH_3), 2.19 Å (CO), and 2.16 Å (PF_3), consistent with the increasing π-acceptor strength of the ligand *trans* to H_2.

The heterolytic H_2 cleavage activation barriers from the H_2-coordinated intermediates follow the trend: **TS_*mer*_PF$_3$** (4.4 (5.1) kcal/mol) < **TS_*mer*_PH$_3$** (6.1 (6.6) kcal/mol) ≈ **TS_*mer*** (7.3 (6.4) kcal/mol) < **TS_*mer*_H$_2$O** (8.1 (8.3) kcal/mol), Figure S7. From a structural perspective, **TS_*mer*_H$_2$O**, exhibits shorter Mn–H distances (1.67–1.70 Å) together with an elongated H–H′ bond (1.03 Å) and a shortened N–H′ bond (1.37 Å), Figure S7. In comparison, **TS_*mer*_PH$_3$** shows longer Mn–H distance (~1.72 Å), a shorter H–H′ bond (0.98 Å), and a slightly elongated N–H′ bond (1.42 Å). In contrast, **TS_*mer*** and **TS_*mer*_PF$_3$** display longer Mn–H distances (1.73–1.76 Å) together with shorter H–H′ bonds (0.94–0.96 Å) and more elongated N–H′ bonds (1.47–1.49 Å), Figure S7.

Notably, the activation barriers correlate with the extent of structural reorganization from the H_2-coordinated intermediates to the transition states. The H_2O system undergoes the largest changes along both H–H′ cleavage and N–H′ bond formation coordinates (Δ(H–H′) = 0.20 Å; Δ(N–H′) = 0.93 Å), consistent with the highest H_2 cleavage activation barrier (8.1 (8.3) kcal/mol). In contrast, the PF_3 system shows the smallest structural changes (Δ(H–H′) = 0.14 Å and Δ(N–H′) = 0.67 Å), resulting in the lowest barrier (4.4 (5.1) kcal/mol). The PH_3 and CO systems exhibit intermediate structural reorganization, with identical H–H′ elongation (Δ(H–H′) = 0.17 Å) and comparable N–H′ formation (Δ(N–H′) = 0.81 Å and 0.75 Å, respectively), consistent with their intermediate activation barriers (6.1 (6.6) kcal/mol and 7.3 (6.4) kcal/mol).

Overall, these results indicate that the higher overall barriers for heterolytic H_2 cleavage primarily arise from the destabilization of the H_2-coordinated intermediates with increasing π-acceptor strength of the ligand *trans* to H_2 in the studied Mn–SNS model systems.

TS_*mer*_H$_2$O	**TS_*mer*_PH$_3$**
$\Delta G^{\ddagger}$ = 8.1 (8.3) kcal/mol	$\Delta G^{\ddagger}$ = 6.1 (6.6) kcal/mol
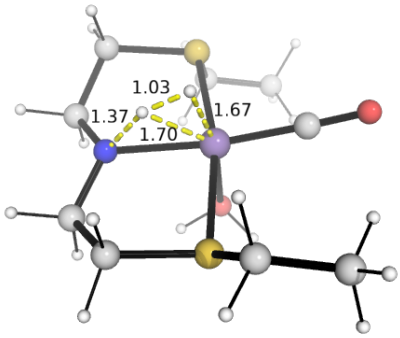	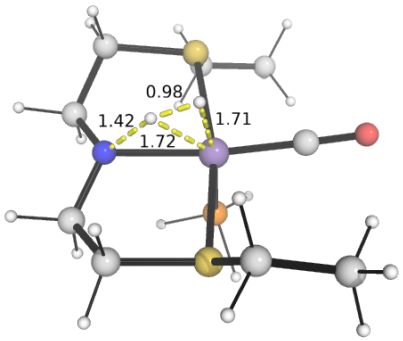
TS_*mer*	**TS_*mer*_PF$_3$**
$\Delta G^{\ddagger}$ = 7.3 (6.4) kcal/mol	$\Delta G^{\ddagger}$ = 4.4 (5.1) kcal/mol

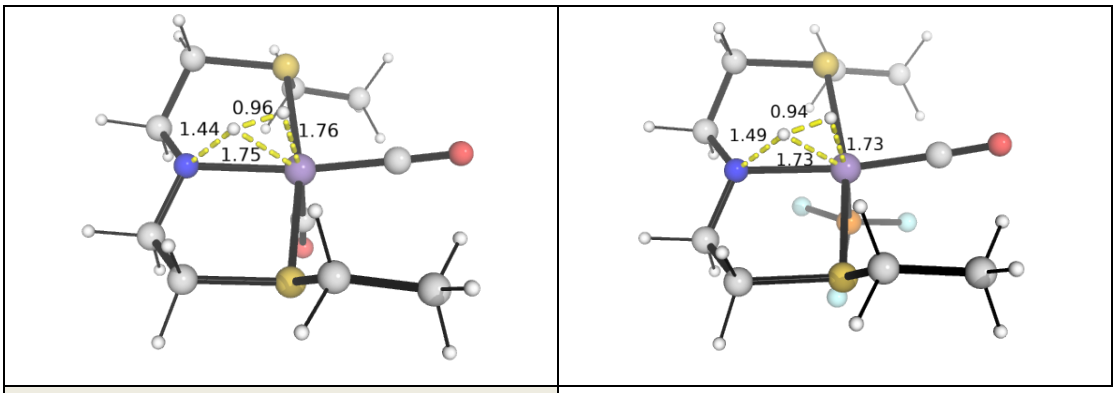

TS_*mer*-PNP

$\Delta G^{\ddagger}$ = 4.3 (5.1) kcal/mol

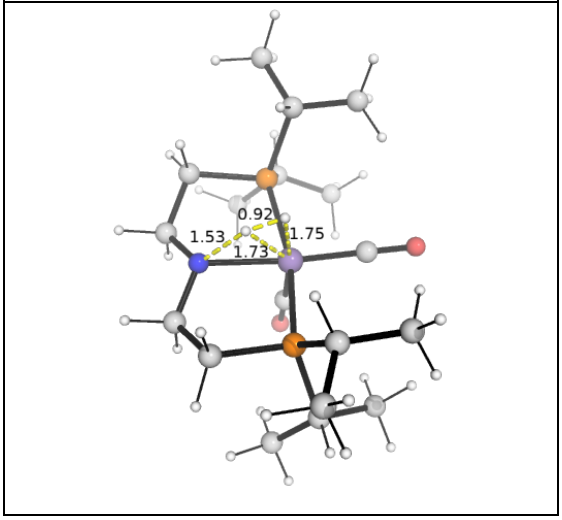

Figure S7. DFT optimized geometries of transition state structures for heterolytic H_2 cleavage in the *mer*-Mn-SNS model systems, where the CO ligand *trans* to the H_2 coordination site is replaced by ligands of varying π-acceptor strength (H_2O, PH_3, PF_3), along with the Mn-PNP system (**TS_*mer*-PNP**). Activation free energies are given in kcal/mol, relative to the corresponding H_2-coordinated intermediates. Selected crucial bond lengths are given in Å. Gibbs energies were computed at SMD(THF)-B3LYP-D3BJ/def2-QZVP//B3LYP-D3BJ/(def2-TZVPPD for Mn + def2-SVP for all other atoms) level of theory. Corresponding free energies computed at the SMD(THF)-MN15/def2-QZVP//B3LYP-D3BJ/(def2-TZVPPD for Mn, def2-SVP for all other atoms) level are given in parentheses.

Section S6. Electronic-structure analysis of H_2 coordination and heterolytic cleavage in the *fac* and *mer* pathways

To further characterize the electronic factors governing H_2 coordination and cleavage, the H_2-coordinated intermediates and the corresponding transition states for heterolytic H_2-cleavage in the *fac* and *mer* pathways were analyzed using frontier molecular orbitals (FMO) and natural population analysis (NPA), Figure S8. The NPA results show only moderate changes in the atomic charges on the Mn center and the amido N atom, accompanied by increasing charge difference between the two H atoms as H_2 cleavage proceeds.

	C-*fac*-H_2	TS_*fac*
ΔG (kcal/mol)	31.4 (20.4)	38.7 (27.9)
DFT Structure	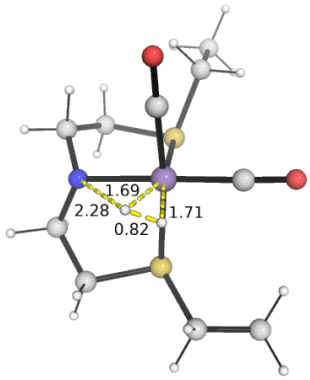	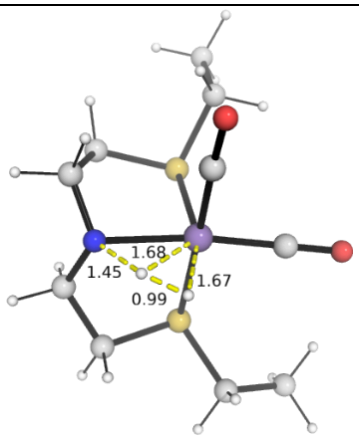
HOMO	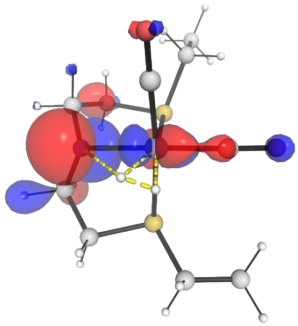	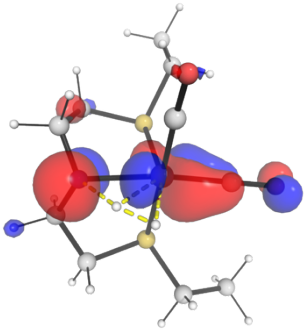
LUMO	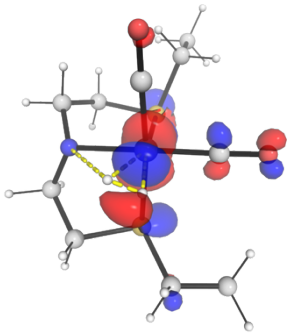	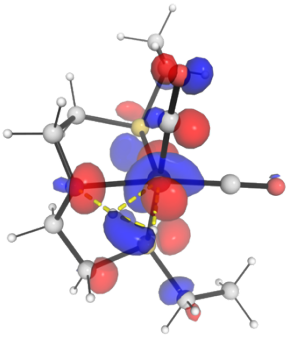
NPA	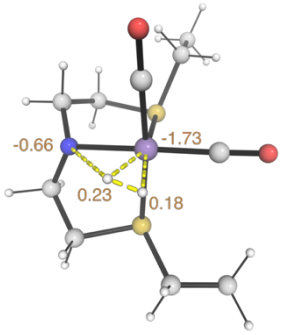	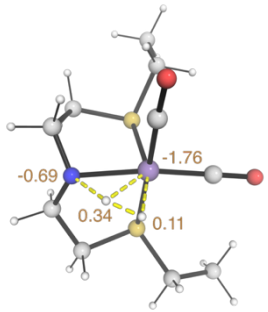
	C-*mer*-H_2	TS_*mer*
ΔG (kcal/mol)	26.5 (16.3)	33.8 (22.7)

DFT Structure	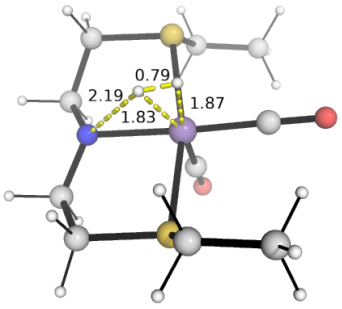	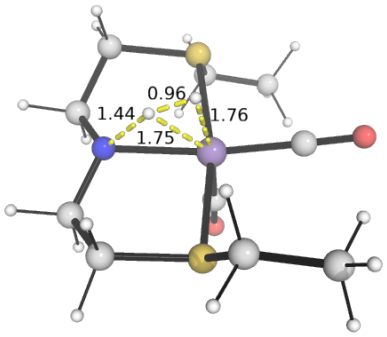
HOMO	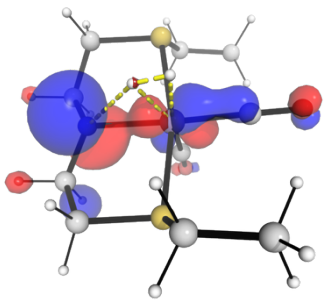	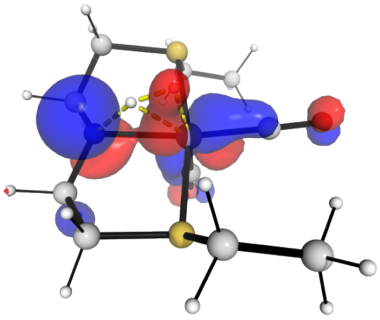
LUMO	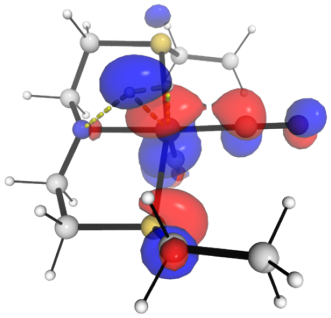	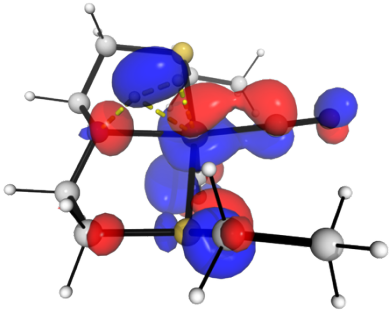
NPA	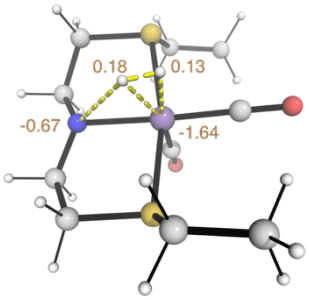	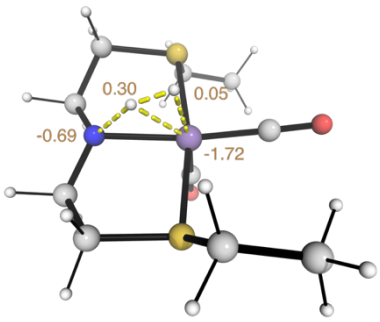

Figure S8. DFT optimized geometries, frontier molecular orbitals (HOMO and LUMO), and natural population analysis (NPA) charges of H_2-coordinated intermediates and heterolytic H_2-cleavage transition states leading to the formation of **1-*fac*** and **1-*mer***. Activation free energies are given in kcal/mol, relative to the **Mn-*fac***. Selected crucial bond lengths are given in Å. Gibbs energies were computed at SMD(THF)-B3LYP-D3BJ/def2-QZVP//B3LYP-D3BJ/(def2-TZVPPD for Mn + def2-SVP for all other atoms) level of theory. Corresponding free energies computed at the SMD(THF)-MN15/def2-QZVP//B3LYP-D3BJ/(def2-TZVPPD for Mn, def2-SVP for all other atoms) level are given in parentheses.

Section S7. Effect of implicit solvation on the optimized structures and heterolytic H_2 activation barriers

To evaluate the sensitivity of the calculated activation barriers for the formation of the active hydride [HMn–NH] complexes to the treatment of solvation during geometry optimization, the key transition structures for heterolytic H_2-cleavage, **TS_*fac*** and **TS_*mer***, were reoptimized using the SMD(THF) solvation model at the B3LYP-D3BJ level with def2-TZVPPD for Mn and def2-SVP for all other atoms.

To quantify the structural changes induced by implicit-solvent geometry optimization, the gas-phase and SMD(THF) optimized transition states were aligned using the *align* function in PyMOL.[1] PyMOL first establishes the correspondence between the two structures using a global dynamic-programming alignment[2] with the default BLOSUM62 scoring matrix.[3] The matched atom pairs are then superimposed by least-squares fitting to minimize the root-mean-square deviation (RMSD) between their Cartesian coordinates. The alignment was then iteratively refined by automatic outlier rejection for up to five cycles.

The superposition yielded RMSD values of 0.014 Å for **TS_*fac*** and 0.027 Å for **TS_*mer***, Figure S9, indicating that implicit-solvent optimization induces only negligible structural changes. Consistent with these small RMSD values, the H_2-cleavage barrier for the *fac* pathway remained unchanged at 13.9 (4.8) kcal/mol, while that for the *mer* pathway lowered moderately from 27.4 (18.5) to 25.4 (18.5) kcal/mol. Thus, implicit-solvent optimization does not alter the qualitative preference for H_2 activation through the *fac* pathway.

TS_*fac*	**TS_*mer***
RMSD = 0.014 Å	RMSD = 0.027 Å
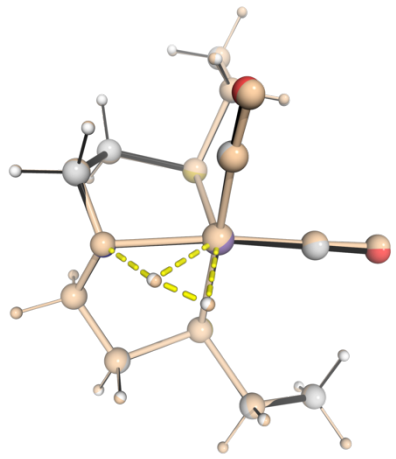	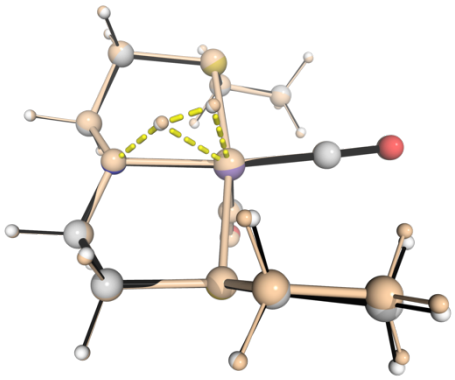

Figure S9. Overlay of the transition states for heterolytic H_2 cleavage leading to the formation of **1-*fac*** and **1-*mer***, optimized in the gas phase at B3LYP-D3BJ/(def2-TZVPPD for Mn + def2-SVP for all other atoms) and in the

implicit solvent phase at SMD(THF)-B3LYP-D3BJ/(def2-TZVPPD for Mn + def2-SVP for all other atoms). The gas-phase optimized structures are shown in the standard atom colors, whereas the SMD(THF) optimized structures are shown in wheat, with the RMSD value given in Å.

Section S8. Effect of explicit THF solvation on H_2 activation barriers

To examine specific solute–solvent interactions beyond those captured by the continuum solvation model, microsolvated models were constructed for the key H_2-activation transition states in both *fac* and *mer* pathways. In each model, one explicit THF molecule was placed in the secondary coordination sphere, followed by full geometry optimization of the entire microsolvated system.

The inclusion of one explicit THF molecule gave activation barriers that are 10.7 (10.1) and 8.8 (10.3) kcal/mol higher than without explicit THF molecule for the *fac* and *mer* pathways, respectively.

As an additional solvent molecule is added to the TS structure, there is a competition between enthalpic favorability due to the formation of H•••O(THF) interaction and the entropic penalty as an additional molecule is added. The entropic penalty is very unfavorable for both the *fac* and *mer* pathways. Therefore, for all subsequent steps, we do not consider the effect of the explicit solvent molecule.

TS_*fac*	**TS_*mer***
$\Delta G^{\ddagger}$ = 13.9 (4.8) kcal/mol	$\Delta G^{\ddagger}$ = 27.4 (18.5) kcal/mol
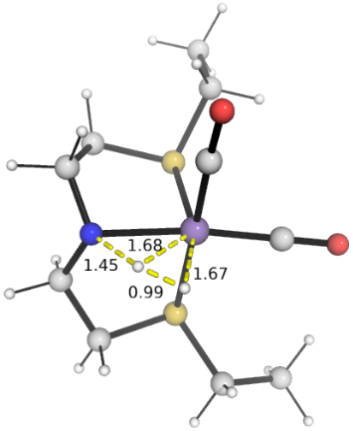	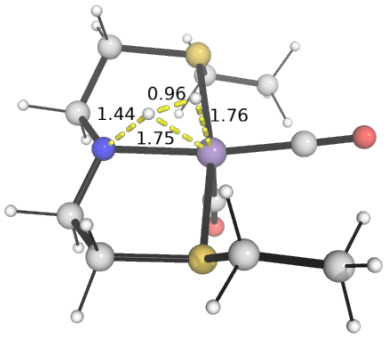
TS_*fac*_THF	**TS_*mer*_THF**
$\Delta G^{\ddagger}$ = 21.1 (12.7) kcal/mol	$\Delta G^{\ddagger}$ = 25.6 (18.0) kcal/mol

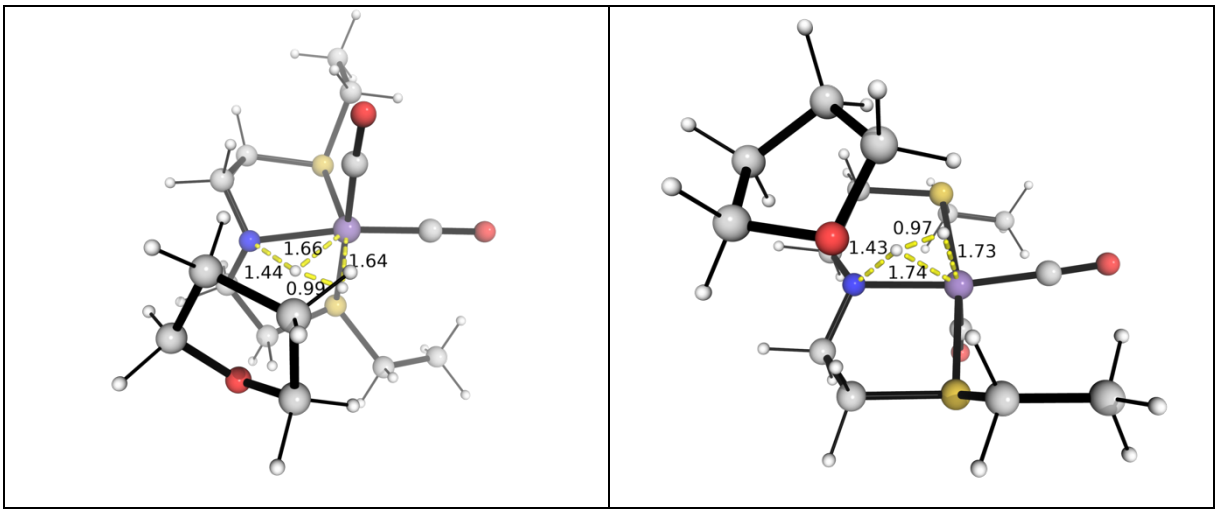

Figure S10. DFT optimized transition state for heterolytic H_2 cleavage leading to the formation of **1-*fac*** and **1-*mer***, computed using the standard gas-phase optimization/SMD(THF) single-point protocol and representative microsolvated models containing one explicit THF molecule. Activation free energies are given in kcal/mol, relative to the corresponding **C-*fac*** or **C-*mer*** intermediate and H_2. Selected crucial bond lengths are given in Å. Gibbs energies were computed at SMD(THF)-B3LYP-D3BJ/def2-QZVP//B3LYP-D3BJ/(def2-TZVPPD for Mn + def2-SVP for all other atoms) level of theory. Corresponding free energies computed at the SMD(THF)-MN15/def2-QZVP//B3LYP-D3BJ/(def2-TZVPPD for Mn, def2-SVP for all other atoms) level are given in parentheses.

Section S9. Effect of the potassium countercation on the formation of 1-*fac* and 1-*mer*

Since K_3PO_4 was used experimentally and potassium-countercation effects have been reported for related anionic Mn(I)-H catalysts, representative K^+-associated structures were examined for both the *fac* and *mer* pathways. In the optimized structures shown in Figure S11, the K^+ ion interacts with the deprotonated amido nitrogen and a carbonyl oxygen in the secondary coordination sphere. Models containing one additional THF molecule coordinated to K^+ were also considered to assess the effect of microsolvation.

C-*fac*_K^+	TS_*fac*_K^+
ΔG = 14.1 (17.0) kcal/mol	ΔG = 32.9 (25.3) kcal/mol

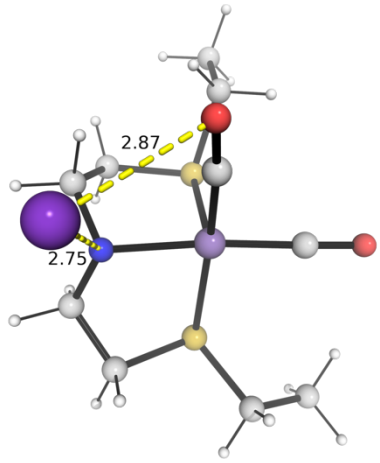	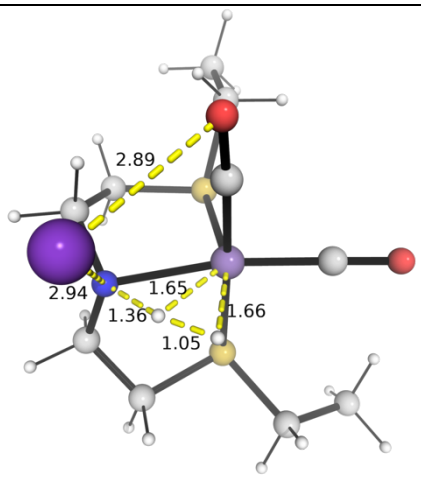
C-*fac*_THF_K$^+$	**TS_*fac*_THF_K$^+$**
ΔG = 15.5 (20.8) kcal/mol	ΔG = 33.4 (28.3) kcal/mol
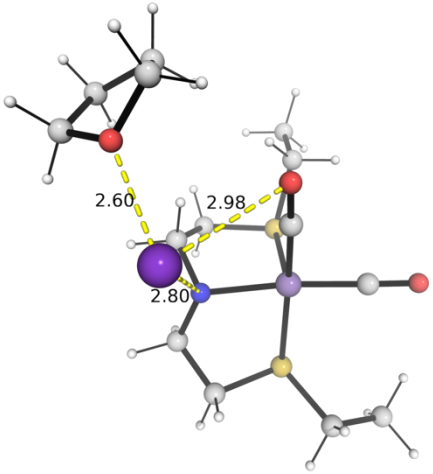	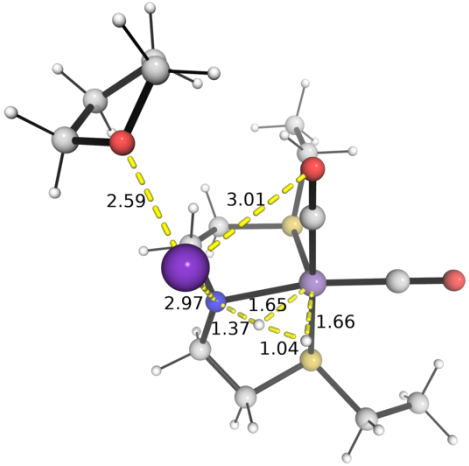
C-*mer*_K$^+$	**TS_*mer*_K$^+$**
ΔG = 1.8 (5.0) kcal/mol	ΔG = 28.9 (24.3) kcal/mol
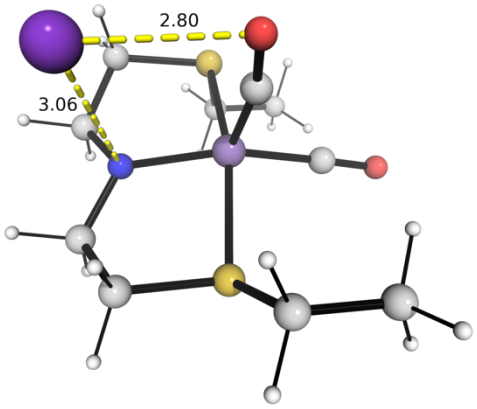	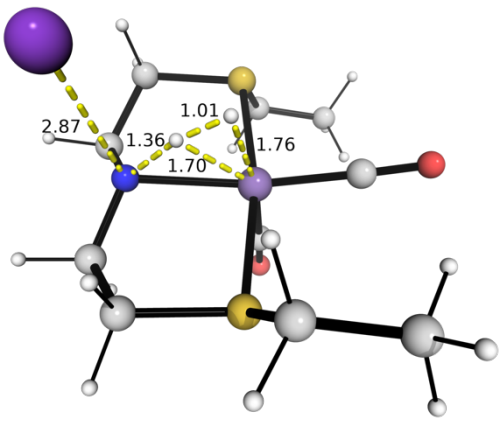
C-*mer*_THF_K$^+$	**TS_*mer*_THF_K$^+$**
ΔG = 1.7 (7.3) kcal/mol	ΔG = 28.3 (25.4) kcal/mol

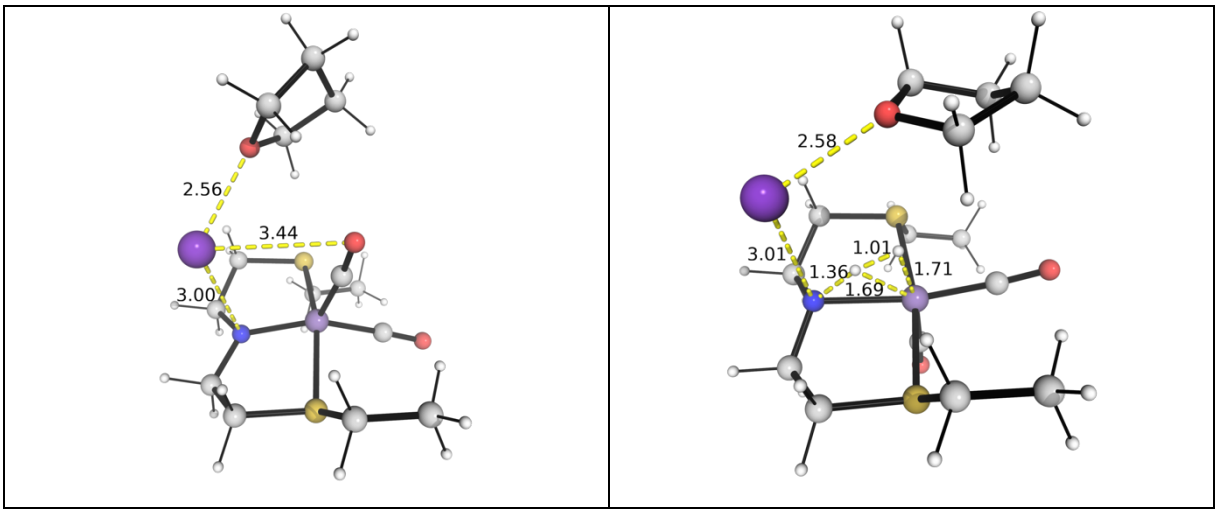

Figure S11. DFT optimized geometries of the K^+-associated intermediates and transition state structures for heterolytic H_2 cleavage leading to the formation of **1-*fac*** and **1-*mer***, together with the corresponding models containing one explicit THF molecule. Activation free energies are given in kcal/mol, relative to the **Mn-*fac*** and the corresponding K^+ and THF components. Selected interatomic distances are given in Å. Gibbs energies were computed at SMD(THF)-B3LYP-D3BJ/def2-QZVP//B3LYP-D3BJ/(def2-TZVPPD for Mn + def2-SVP for all other atoms) level of theory. Corresponding free energies computed at the SMD(THF)-MN15/def2-QZVP//B3LYP-D3BJ/(def2-TZVPPD for Mn, def2-SVP for all other atoms) level are given in parentheses.

Section S10. Energetic span analysis and turnover frequency estimation

To quantitatively assess the kinetics of the three sequential reaction stages, turnover frequencies were estimated using the dominant energetic-span δE approximation[4]:

$$\mathrm{TOF} \approx \frac{k_B T}{h} \exp\left(-\frac{\delta E}{RT}\right)$$

where k_B is the Boltzmann constant, h is the Planck constant, R is the gas constant, and T is the reaction temperature. The corresponding turnover number after 24 h was estimated as

$$\mathrm{TON}_{24\mathrm{h}} = \mathrm{TOF} \times 86400$$

Table S2. Energetic spans (δE), turnover-frequency (TOF) estimates, and corresponding 24-h turnover numbers (TON) for the three sequential reactions at 393.15 K. Values outside and inside parentheses were obtained using the B3LYP-D3BJ and MN15 energetic spans, respectively.

Reaction	**TDI**	**TDTS**	***δE*** **(kcal/mol)**	**Estimated TOF (s^{-1})**	**Estimated 24-h TON**
CO_2 → HCOOH	***3′-fac***	**TS2_*fac***	28.3 (28.0)	1.4×10^{-3} (2.4×10^{-3})	124 (208)
Morpholine + HCOOH	**6**	**TS6**	25.9 (27.2)	3.4×10^{-2} (6.5×10^{-3})	2925 (562)

→ *N*-formylmorpholine					
N-formylmorpholine → methanol	**1-*mer***	**TS_*mer***	35.0 (32.3)	2.9×10^{-7} (9.0×10^{-6})	0.02 (0.8)

As summarized in Table S2, the predicted TOFs indicate that CO_2 hydrogenation to HCOOH and the formation of *N*-formylmorpholine are much faster than the final hydrogenation of *N*-formylmorpholine to methanol. Thus, the final hydrogenation step is predicted to be the rate-limiting step of the overall reaction. Both B3LYP-D3BJ and MN15 give the same qualitative trend, although the absolute TOF values differ because of the exponential dependence on the energetic span. The calculated TOFs represent idealized intrinsic standard-state estimates and do not account for concentration effects, H_2 pressure, catalyst speciation, or catalyst deactivation.

To reconcile these differences, we first convert the experimental TON into an average TOF:

For TON $= 60$, after 24 h (reaction time):

$$\mathrm{TOF}_{\mathrm{exp,avg}} = \frac{60}{24 \times 3600} = 6.94 \times 10^{-4}\ \mathrm{s}^{-1}.$$

At $120^{\circ}\mathrm{C}$ (393.15 K), this corresponds to an apparent energetic span of

$$\delta G_{\mathrm{exp}} = RT\ln\left(\frac{k_{\mathrm{B}}T/h}{\mathrm{TOF}_{\mathrm{exp}}}\right) \approx 28.9\ \mathrm{kcal\ mol}^{-1}.$$

Thus, experiment effectively indicates a span near $29\ \mathrm{kcal\ mol}^{-1}$, *assuming* approximately constant activity over 24 h.

Next, we correct for the effect of pressure, the experiment used 60 atm H_2 and 10 atm CO_2. If one H_2 molecule enters the cycle between the TDI and TDTS, the pressure correction is

$$\delta G_{\mathrm{span}}(p) = \delta G^{\circ}_{\mathrm{span}} - RT\ln\left(\frac{p_{\mathrm{H_2}}}{p^{\circ}}\right).$$

At 393.15 K and 60 atm:

$$RT\ln(60) = 3.20\ \mathrm{kcal\ mol}^{-1}.$$

Therefore:

Functional result	Standard-state span	Span at 60 atm H_2	Corrected TOF	Idealized 24-h TON
B3LYP-D3	35.0 kcal/mol	31.8 kcal/mol	$1.7 \times 10^{-5}\ s^{-1}$	1.5
MN15	32.3 kcal/mol	29.1 kcal/mol	$5.4 \times 10^{-4}\ s^{-1}$	47
Experiment	—	$\sim$ 28.9 kcal/mol	$6.9 \times 10^{-4}\ s^{-1}$	60

We observed that using MN15 functional, the pressure-corrected TON prediction is approximately 47, compared with the experimental value of 60. The residual difference is only:

$$29.1 - 28.9 = 0.2\ \text{kcal mol}^{-1},$$

which is well within DFT accuracy errors. This is effectively a rate factor of about 1.3 and is essentially quantitative agreement given the approximations.

The first functional remains slower than experiment by a factor of approximately 40, corresponding to an overestimation of the effective span by about 2.9 kcal mol^{-1}. This is within a plausible DFT free-energy error, but it shows the strong functional sensitivity: the two functionals differ by 2.7 kcal mol^{-1}, which translates into a factor of about 32 in TOF at 393.15 K.

Section S11. Optimized structures and absolute energies, zero-point energies

Geometries of all optimized structures (in *.xyz* format with their associated energy in Hartrees) are included in a separate folder named *DFT_optimized_xyz*. All these data have been deposited and uploaded to zenodo.org under https://zenodo.org/records/21414490.

Absolute values (in Hartrees) for SCF energy, zero-point vibrational energy (ZPE), enthalpy and quasi-harmonic Gibbs free energy (at 120°C/393.15 K) for optimized structures are given below. Single point corrections in SMD tetrahydrofuran (THF) using B3LYP-D3BJ/def2-QZVP and MN15/def2-QZVP level of theory are also included.

Struc-ture	E/au	ZPE/au	H/au	T.S/au	qh-G/au	SP B3LYP-D3BJ/def2-QZVP	SP MN15/def2-QZVP
CO	-113.225741	0.005114	-113.216267	0.026461	-113.242728	-113.3653483	-113.300282
HBr	-2574.788988	0.005943	-2574.77869	0.026597	-2574.80528	-2574.848389	-2575.235776
H_2	-1.173933	0.009939	-1.159636	0.016445	-1.176082	-1.18012021	-1.169521
K_2HPO_4	-1842.492373	0.027938	-1842.450042	0.060385	-1842.509	-1843.275107	-1842.919463
K_3PO_4	-2441.807196	0.017501	-2441.77353	0.066134	-2441.83751	-2442.673803	-2442.262913
KBr	-3173.811684	0.000506	-3173.80601	0.034644	-3173.84065	-3174.299558	-3174.630058
H_2O	-76.35889	0.021232	-76.332658	0.025345	-76.358003	-76.47961256	-76.430709
HCOOH	-189.622499	0.033963	-189.582705	0.034797	-189.617502	-189.8717468	-189.757182
morpholine	-287.60308	0.134778	-287.45806	0.045962	-287.504025	-287.960869	-287.739828
CO_2	-188.44468	0.011774	-188.427908	0.030177	-188.458085	-188.6833768	-188.57627
CH_3OH	-115.634996	0.051037	-115.577955	0.033241	-115.611197	-115.7935353	-115.7078
CH_2O	-114.417332	0.026534	-114.385656	0.03079	-114.416446	-114.5679737	-114.489229
K^+	-599.682772	0	-599.679659	0.01966	-599.699319	-599.853821	-599.797623
THF	-232.294111	0.116354	-232.168581	0.044157	-232.212236	-232.582099	-232.398933
Mn-*fac*	-5232.124546	0.297681	-5231.78734	0.119385	-5231.89902	-5233.390588	-5233.169686
Mn-*mer*	-5232.12897	0.29815	-5231.79136	0.11705	-5231.902	-5233.388533	-5233.168858
A-*fac*	-5118.871347	0.289219	-5118.54635	0.107606	-5118.64908	-5119.990023	-5119.839872
B-*fac*	-5118.86125	0.28881	-5118.53646	0.1087	-5118.6397	-5119.983682	-5119.833422

C-*fac*	-2543.978032	0.272309	-2543.67267	0.10074	-2543.76883	-2545.036101	-2544.497168
C-*fac*-H$_2$	-2545.164391	0.289316	-2544.8406	0.102504	-2544.93881	-2546.224321	-2545.689591
TS_*fac*	-2545.154974	0.288025	-2544.83361	0.100451	-2544.92991	-2546.212151	-2545.677112
1-*fac*	-2545.19644	0.295749	-2544.8671	0.101351	-2544.96394	-2546.26668	-2545.724589
TS_*iso*	-2543.975763	0.271771	-2543.67175	0.09878	-2543.7663	-2545.032694	-2544.493632
C-*mer*	-2544.009331	0.272842	-2543.70358	0.100667	-2543.79957	-2545.066062	-2544.52804
C-*mer*-H$_2$	-2545.17161	0.288637	-2544.84832	0.102572	-2544.94665	-2546.231556	-2545.695576
TS_*mer*	-2545.165065	0.287623	-2544.84408	0.100407	-2544.94038	-2546.219631	-2545.685081
1-*mer*	-2545.198396	0.297987	-2544.86667	0.101381	-2544.96368	-2546.265042	-2545.725123
2-*fac*	-2733.656656	0.308892	-2733.30824	0.117985	-2733.41843	-2734.957085	-2734.306702
TS1_*fac*	-2733.652508	0.309085	-2733.30479	0.114881	-2733.4128	-2734.951827	-2734.296477
3-*fac*	-2733.659638	0.313258	-2733.30783	0.113113	-2733.41535	-2734.962343	-2734.304919
TS2_*fac*	-2733.64738	0.309196	-2733.30002	0.111627	-2733.40681	-2734.949248	-2734.292891
3'-*fac*	-2733.680204	0.311723	-2733.3295	0.116477	-2733.43871	-2734.983035	-2734.329177
4-*fac*	-2734.847891	0.327594	-2734.48014	0.116428	-2734.59068	-2736.149458	-2735.491143
TS3_*fac*	-2734.845888	0.326179	-2734.48027	0.115775	-2734.58976	-2736.144819	-2735.483869
5-*fac*	-2734.859345	0.331757	-2734.48765	0.117616	-2734.59833	-2736.159654	-2735.496914
6	-287.603076	0.134767	-287.458065	0.045966	-287.504035	-287.960859	-287.739822
7	-666.891094	0.207275	-666.660643	0.080722	-666.737116	-667.7232759	-667.272831
TS4	-666.885515	0.207955	-666.656781	0.073233	-666.727464	-667.7182308	-667.264629
8	-666.897002	0.209623	-666.666763	0.071458	-666.736604	-667.7296065	-667.282169
TS5	-666.895213	0.206218	-666.668668	0.070643	-666.737793	-667.7244934	-667.279093
9	-666.895504	0.208628	-666.665932	0.072262	-666.736464	-667.7245413	-667.280362
10	-477.231176	0.172638	-477.042955	0.05916	-477.101224	-477.8297735	-477.503324
11	-666.884678	0.209031	-666.654167	0.074864	-666.725976	-667.7149341	-667.270667
TS6	-666.876137	0.203915	-666.651416	0.072863	-666.721746	-667.7084669	-667.256245
12	-666.908407	0.206236	-666.678508	0.080865	-666.755487	-667.7462614	-667.294137
13	-590.525511	0.18127	-590.324964	0.071171	-590.392988	-591.260008	-590.855542
14	-400.874404	0.144834	-400.716582	0.053597	-400.769499	-401.3710602	-401.082965
15-*fac*	-2946.101641	0.442662	-2945.61119	0.136257	-2945.73744	-2947.649899	-2946.81691

TS4_*fac*	-2946.072491	0.439763	-2945.58633	0.130531	-2945.70888	-2947.615244	-2946.781201
16-*fac*	-2946.072961	0.441589	-2945.58435	0.132302	-2945.70824	-2947.615743	-2946.783105
17-*fac*	-2947.278895	0.465481	-2946.76447	0.137694	-2946.89269	-2948.837102	-2947.99999
TS5_*fac*	-2947.171379	0.460058	-2946.66208	0.138922	-2946.79094	-2948.72794	-2947.875451
18-*fac*	-2947.281513	0.465597	-2946.76564	0.140068	-2946.89679	-2948.826326	-2947.979125
19-*fac*	-2946.096176	0.442158	-2945.60595	0.13704	-2945.73265	-2947.64749	-2946.815962
TS6_*fac*	-2946.051801	0.440421	-2945.56426	0.130894	-2945.68806	-2947.592731	-2946.747642
20-*fac*	-2946.055137	0.440052	-2945.56496	0.143473	-2945.69699	-2947.59698	-2946.757903
21-*fac*	-2659.643577	0.328095	-2659.27767	0.110336	-2659.38323	-2660.849896	-2660.22226
TS7_*fac*	-2659.643063	0.323714	-2659.28198	0.109352	-2659.38663	-2660.847251	-2660.221198
22-*fac*	-2659.647945	0.326107	-2659.28349	0.111777	-2659.39026	-2660.848586	-2660.224942
2-*mer*	-2733.658159	0.311059	-2733.30732	0.118556	-2733.41787	-2734.956608	-2734.304837
TS1_*mer*	-2733.657739	0.3112	-2733.30782	0.115411	-2733.41596	-2734.955633	-2734.302397
3-*mer*	-2733.672755	0.311378	-2733.32311	0.111855	-2733.42975	-2734.973353	-2734.317238
TS2_*mer*	-2733.66148	0.3092	-2733.31415	0.112549	-2733.42088	-2734.961396	-2734.305413
3pr-*mer*	-2733.695283	0.312808	-2733.34385	0.113225	-2733.45163	-2734.995653	-2734.342587
4-*mer*	-2734.86283	0.332726	-2734.49004	0.115098	-2734.6001	-2736.162247	-2735.496776
TS3_*mer*	-2734.860766	0.330066	-2734.49124	0.114775	-2734.60038	-2736.157892	-2735.491925
5-*mer*	-2734.863996	0.333478	-2734.49062	0.11662	-2734.60071	-2736.161236	-2735.497208
TS2pr_*mer**	-2733.657632	0.30443	-2733.31398	0.11361	-2733.4226	-2734.954279	-2734.298242
4pr-*mer*	-2733.652945	0.308406	-2733.30487	0.119019	-2733.41596	-2734.952027	-2734.297203
15-*mer*	-2946.102519	0.444724	-2945.60984	0.135624	-2945.73583	-2947.650688	-2946.817226
TS7_*mer*	-2946.092136	0.443908	-2945.60198	0.130034	-2945.72408	-2947.635802	-2946.798871
16-*mer*	-2946.092169	0.443959	-2945.60121	0.132337	-2945.72516	-2947.635981	-2946.799283
TS8_*mer*	-2946.088763	0.437477	-2945.60474	0.130251	-2945.72733	-2947.629947	-2946.794563
17-*mer*	-2946.090427	0.441467	-2945.60158	0.133455	-2945.72629	-2947.632306	-2946.797396
15	-402.055486	0.167861	-401.873653	0.055229	-401.928499	-402.556129	-402.263336
18-*mer*	-2947.268889	0.463285	-2946.75637	0.137769	-2946.88465	-2948.830565	-2948.00131
TS9_*mer*	-2947.177699	0.461031	-2946.66765	0.137091	-2946.79557	-2948.7345	-2947.884136

19-*mer*	-2947.288124	0.463129	-2946.77384	0.144347	-2946.9072	-2948.838154	-2947.99197
20-*mer*	-2946.105097	0.444903	-2945.6123	0.134966	-2945.73793	-2947.651806	-2946.818183
TS10_*mer*	-2946.077131	0.445551	-2945.58531	0.129287	-2945.7074	-2947.620651	-2946.780602
21-*mer*	-2946.078202	0.443439	-2945.58821	0.128965	-2945.71054	-2947.620369	-2946.780653
TS11_*mer*	-2946.062938	0.438064	-2945.57855	0.127556	-2945.70016	-2947.604938	-2946.762432
22-*mer*	-2946.119707	0.446196	-2945.62703	0.129332	-2945.74945	-2947.658165	-2946.82479
23-*mer*	-2659.671018	0.326507	-2659.30502	0.116711	-2659.41502	-2660.87102	-2660.246802
C-*mer*-H_2-PNP	-2747.104013	0.534452	-2746.53662	0.089388	-2746.62218	-2748.494112	-2747.619787
TS_*mer*-PNP	-2747.100045	0.533369	-2746.53446	0.088294	-2746.61894	-2748.486558	-2747.610908
C-*mer*-H_2_H_2O	-2508.271863	0.304384	-2507.9319	0.103936	-2508.03197	-2509.292529	-2508.778139
TS_*mer*_H_2O	-2508.258372	0.303113	-2507.92074	0.101949	-2508.01914	-2509.279012	-2508.764276
C-*mer*-H_2_PH_3	-2774.973995	0.307644	-2774.63056	0.10404	-2774.73104	-2776.026747	-2775.456007
TS_*mer*_PH_3	-2774.965694	0.306279	-2774.62473	0.102342	-2774.72349	-2776.016351	-2775.444702
C-*mer*-H_2_PF_3	-3072.582181	0.291574	-3072.25181	0.112102	-3072.3588	-3074.041523	-3073.365383
TS_*mer*_PF_3	-3072.577461	0.290569	-3072.24925	0.110901	-3072.35466	-3074.033944	-3073.356658
C-*fac*_smd	-2543.996137	0.272082	-2543.69104	0.100524	-2543.78707	-2545.036598	-2544.497401
TS_*fac*_smd	-2545.170447	0.287865	-2544.84929	0.100341	-2544.94547	-2546.212578	-2545.677401
1-*fac*_smd	-2545.223740	0.295594	-2544.89451	0.102016	-2544.99153	-2546.267697	-2545.725077
TS_*iso*_smd	-2543.992241	0.271293	-2543.68856	0.099805	-2543.78353	-2545.032947	-2544.493769
C-*mer*_smd	-2544.024731	0.27258	-2543.71922	0.100844	-2543.81525	-2545.065569	-2544.528203

TS_*mer*_smd	-2545.179969	0.287318	-2544.85930	0.100428	-2544.95557	-2546.222244	-2545.685276
1-*mer*_smd	-2545.225255	0.29788	-2544.89382	0.100453	-2544.99035	-2546.269138	-2545.726066
C-*fac*_THF	-2776.314390	0.392471	-2775.87975	0.119757	-2775.99365	-2777.642353	-2776.922313
TS_*fac*_THF	-2777.466561	0.406304	-2777.01629	0.128166	-2777.13516	-2778.801643	-2778.084466
1-*fac*_THF	-2777.518517	0.414258	-2777.06037	0.127721	-2777.17911	-2778.861054	-2778.132974
C-*mer*_THF	-2776.323989	0.391448	-2775.88923	0.126016	-2776.00670	-2777.656930	-2776.935364
TS_*mer*_THF	-2777.476605	0.405887	-2777.02663	0.128804	-2777.14582	-2778.811904	-2778.091814
1-*mer*_THF	-2777.510521	0.412257	-2777.05411	0.128434	-2777.17305	-2778.854791	-2778.133723
Mn-*fac*_K+	-5831.574766	0.299322	-5831.23279	0.128666	-5831.35177	-5833.282829	-5833.000382
C-*fac*_K^+	-3143.718626	0.273317	-3143.40916	0.109537	-3143.51271	-3144.920246	-3144.317919
TS_*fac*_K^+	-3144.886780	0.289066	-3144.56123	0.109439	-3144.66500	-3146.088481	-3145.492261
1-*fac*_K^+	-3144.943906	0.295386	-3144.61181	0.110309	-3144.71599	-3146.146008	-3145.550307
C-*mer*_K^+	-3143.738359	0.273666	-3143.42880	0.109246	-3143.53161	-3144.940711	-3144.337850
TS_*mer*_K^+	-3144.882212	0.288082	-3144.55737	0.110683	-3144.66179	-3146.093426	-3145.492509
1-*mer*_K^+	-3144.944105	0.295114	-3144.61232	0.109753	-3144.71630	-3146.148772	-3145.551528
Mn-*fac*_THF_K^+	-6063.902754	0.416957	-6063.43229	0.161062	-6063.57588	-6065.884222	-6065.41491
C-*fac*_THF_K^+	-3376.051777	0.391686	-3375.61332	0.136933	-3375.73918	-3377.524997	-3376.735589
TS_*fac*_THF_K^+	-3377.221358	0.4075	-3376.76681	0.136322	-3376.89264	-3378.694797	-3377.911402

1-*fac*_THF_K$^+$	-3377.272610	0.414041	-3376.81145	0.13552	-3376.93717	-3378.751396	-3377.966866
C-*mer*_THF_K$^+$	-3376.073553	0.391837	-3375.63519	0.13709	-3375.76038	-3377.547552	-3376.757709
TS_*mer*_THF_K$^+$	-3377.221066	0.406732	-3376.76706	0.13801	-3376.89356	-3378.701810	-3377.914765
1-*mer*_THF_K$^+$	-3377.274943	0.413259	-3376.81437	0.137504	-3376.94080	-3378.752559	-3377.967743

Section S12. References

Full reference Gaussian 16:

M. J. Frisch, G. W. Trucks, H. B. Schlegel, G. E. Scuseria, M. A. Robb, J. R. Cheeseman, G. Scalmani, V. Barone, B. Mennucci, G. A. Petersson, H. Nakatsuji, M. Caricato, X. Li, H. P. Hratchian, A. F. Izmaylov, J. Bloino, G. Zheng, J. L. Sonnenberg, M. Hada, M. Ehara, K. Toyota, R. Fukuda, J. Hasegawa, M. Ishida, T. Nakajima, Y. Honda, O. Kitao, H. Nakai, T. Vreven, J. A. Montgomery Jr., J. E. Peralta, F. Ogliaro, M. Bearpark, J. J. Heyd, E. Brothers, K. N. Kudin, V. N. Staroverov, R. Kobayashi, J. Normand, K. Raghavachari, A. Rendell, J. C. Burant, S. S. Iyengar, J. Tomasi, M. Cossi, N. Rega, J. M. Millam, M. Klene, J. E. Knox, J. B. Cross, V. Bakken, C. Adamo, J. Jaramillo, R. Gomperts, R. E. Stratmann, O. Yazyev, A. J. Austin, R. Cammi, C. Pomelli, J. W. Ochterski, R. L. Martin, K. Morokuma, V. G. Zakrzewski, G. A. Voth, P. Salvador, J. J. Dannenberg, S. Dapprich, A. D. Daniels, Ö. Farkas, J. B. Foresman, J. V. Ortiz, J. Cioslowski and D. J. Fox, *Gaussian 16, Revision B.01*, Gaussian, Inc., Wallingford CT, 2016.

1. Schrödinger, LLC, The PyMOL Molecular Graphics System, Version 1.8, 2015.
2. S. B. Needleman and C. D. Wunsch, A General Method Applicable to the Search for Similarities in the Amino Acid Sequence of Two Proteins, *J. Mol. Biol.* 1970, **48**, 443–453.
3. S. Henikoff and J. G. Henikoff, Amino Acid Substitution Matrices from Protein Blocks, *Proc. Natl. Acad. Sci. U. S. A.*, 1992, **89**, 10915–10919.

4. S. Kozuch and S. Shaik, How to Conceptualize Catalytic Cycles? The Energetic Span Model, *Acc. Chem. Res.* 2011, **44**, 101–110.